Contents lists available at ScienceDirect

# **Powder Technology**

journal homepage: www.elsevier.com/locate/powtec



# DEM modeling of fine powder convection in a continuous vibrating bed reactor



Julia Hartig<sup>a</sup>, Hannah C. Howard <sup>a,b</sup>, Tanner J. Stelmach<sup>a</sup>, Alan W. Weimer <sup>a,\*</sup>

- <sup>a</sup> Department of Chemical and Biological Engineering, University of Colorado Boulder, Boulder, CO 80309, USA
- <sup>b</sup> Department of Chemical and Biomolecular Engineering, Georgia Tech, Atlanta, GA 30332, USA

#### ARTICLE INFO

Article history: Received 26 November 2020 Received in revised form 12 February 2021 Accepted 15 March 2021 Available online 19 March 2021

Keywords:
Cohesive powders
Discrete element simulation
Atomic layer deposition
Fast fourier transform
Vibrating system

#### ABSTRACT

Continuous vibrating spatial particle ALD reactors were developed to achieve high powder throughput while minimizing reactor footprint. Unlike fluidized bed reactors, continuous vibrating spatial particle ALD reactors operate below fluidization, using linear vibration to convey particles through alternating regions of precursor gas. Fine powder convection in these vibrating bed reactors is still not well understood, so cohesive discrete-element-method (DEM) simulations were performed to investigate the solids flow behavior. Using a Fast Fourier Transform (FFT) algorithm, we constructed a sum-of-sines model for the reactor kinematics based on accelerometer data. Accelerometer results and DEM simulations revealed the role of high-frequency excitations and need for backsliding and sticking avoidance in horizontal conveyors at low-g accelerations. From these observations, we propose a novel sawtooth excitation to enable convection of cohesive fine powders at low flow velocities. The model results were compared to data from an in-house continuous vibrating spatial particle ALD reactor.

© 2021 Elsevier B.V. All rights reserved.

## 1. Introduction

Particle atomic layer deposition (ALD) is a coating technique that uses sequential gas–solid reactions to deposit thin films on particle substrates [1]. Nanoscale conformal and pinhole-free films can be produced using a series of self-limiting heterogeneous half-reactions [2,3]. ALD can be used to deposit many kinds of coating chemistries on a variety of substrate materials, making its way into diverse fields such as catalysis, lighting, semiconductors, and batteries [1,4]. The fast kinetics of a variety of ALD chemistries, particularly for metal oxide deposition, allow nanoscale coatings to be produced at a competitive price point. Particle ALD has produced high quality ultrathin (<3 nm) alumina films with unparalleled atomic-level thickness and conformality control on the commercial scale [1].

Increasing the production rate in particle ALD is vital to its adoption in new markets. The ALD coating process is typically performed on particle substrates using rotary drum reactors [5] or fluidized bed reactors [6–8]. These batch systems have demonstrated high coating uniformity and precursor utilization but suffer from low particle throughput. Achieving multiple cycles of ALD in a high-throughput batch setup would require multiple reactors in series, leading to a large system footprint and substantial overhead costs. By contrast, continuous vibrating spatial particle ALD, where particles flow through alternating regions of precursor gas via directional vibration, enables high powder

throughput while maintaining low capital costs. Thus, continuous spatial particle ALD is a promising technique when maximizing production is a high priority and the number of ALD cycles being performed is small.

In both batch and continuous particle ALD, vibration is incorporated to improve gas flow uniformity through the powder bed. Vibration leads to agitation in dense particle regions, helping to break up plugs and prevent particle interlocking [9,10]. Mechanical, acoustic and magnetic agitation are commonly used in fine powder fluidized beds to destabilize cohesive channels and suppress slugging [11-13]. Bed agitation also promotes efficient gas-particle and particle-particle mixing [14]. In a continuous vibrating spatial particle ALD reactor, linear vibration transports particles through alternating gas zones with moderate-frequency, low-amplitude oscillations [15]. Thus, optimized vibratory convection can accomplish two goals simultaneously: transporting particles and promoting gas-solid contact. Prior experiments and simulations have demonstrated that higher vibration intensities lead to bed compaction [16,17] and smaller mean agglomerate sizes in fluidized beds of fine cohesive powders [18–20]. It is unknown whether these trends with vibration intensity can be extended to a continuous spatial particle ALD reactor, where vibration is two-dimensional and gas velocities are below fluidization.

The dual role of vibration, among other features, makes continuous spatial particle ALD complex as compared to its fluidized bed predecessor. Although previous works cover many reactor-scale experimental [4] and numerical [21–23] studies of spatial ALD on flat substrates, continuous vibrating spatial ALD on particle substrates was only developed and commercialized within the last decade [24]. As a result, the

<sup>\*</sup> Corresponding author. *E-mail address:* alan.weimer@colorado.edu (A.W. Weimer).

behavior of particles inside continuous vibrating reactors (CVRs) is still not well understood. Modeling results for an ALD system where a powder substrate is driven by vibratory convection are lacking in literature. Some studies have been published on a continuous spatial particle ALD system driven by pneumatic convection [25], but to the authors' knowledge, there are no published papers on CVR-ALD.

The relationship between vibration intensity and time-averaged powder convection velocity in a vibratory conveyor is still not well defined. Historically, algebraic expressions [15,26] have been developed and single-particle or rigid body simulations [27–31] have been performed to investigate this behavior, but empirically fitted coefficients and lack of particle-particle collision treatment prevent these models from being predictive. DEM simulations have also been used to predict mean convection velocity of coarse powders in vibrating sieves [32], banana screens [33], and vibratory bowl feeders [34]. Prior investigations into linear vibratory conveyors and feeders have focused on particle shape [35], the so-called "reactive effect" [36], vibrator stall [37], and particle dispersion [38].

However, DEM simulations of fine powders in vibratory conveyors, where cohesive effects play a significant role, are still needed to investigate and improve powder flow behavior in CVR-ALD. Processing of fine (Geldart A) and ultrafine (Geldart C) powders are of great interest to more than just the ALD community [39]. Lessons learned on improving the flowability of powders in CVR-ALD reactors will have pertinence to other fine powder processes such as coating, drying and granulation [40–43]. DEM simulations, and ultimately CFD-DEM, could answer some key questions about particle-particle and gas-particle interactions during linear vibration. Here, we investigate the key particle-particle and particle-wall interactions in CVR-ALD using DEM modeling.

#### 2. Methods

## 2.1. Discrete Element Method Equations

In the discrete element method, individual particles are tracked by solving Newton's equation of motion for translation velocity  $\vec{u}$  i and rotational velocity  $\vec{\omega}$  i of each particle i with mass  $m^i$ :

$$m^{i}\frac{d\vec{u}^{i}}{dt} = \sum_{i} \vec{F}^{i} = m^{i}\vec{g}^{i} + \sum_{i} \vec{F}_{C}^{i,j} + \vec{F}_{D}^{i} + \sum_{k} \vec{F}_{vdW}^{i,k}$$
 (1)

$$l^{i}\frac{d\vec{\omega}^{i}}{dt} = \sum_{i} \vec{r}^{i,j} \times \vec{F}_{C}^{i,j}$$
 (2)

where  $\overrightarrow{g}$  i is the gravitational acceleration;  $\sum_j \vec{F}_C^{i,j}$  the sum of all P–P and

P–W contact forces with each collision partner j;  $\bar{F}_D^i$  the particle-fluid drag force;  $\sum_k \bar{F}_{vdW}^{i,k}$  the sum of all van der Waals cohesive forces with

each cohesive partner k;  $I^i$  the particle's moment of inertia;  $\sum \bar{T}^i$  the total torque; and  $\bar{r}^{i,j}$  the displacement vector from the center of particle i to its contact point with collision partner j. Pure granular flow (neglecting particle-fluid drag force term  $\bar{F}_D^i$ ) will be considered in this study. This approach is common when modeling systems with gas velocities much lower than the minimum fluidization velocity  $u_{mf}$  [16] and has shown good agreement with experiments when modeling vibratory systems [9,44,45], including vibratory conveyors [38]. CVR-ALD reactors operate below fluidization, resulting in fluid-particle drag forces that are small compared to cohesive forces (Fig. 1). At sufficiently low reactor pressures P < 10 Torr typical of fluidized bed particle ALD, where the particle Knudsen number  $Kn_p$  (ratio of gas mean free path to particle diameter) exceeds 1 [18,46] and drag forces are small at the relative

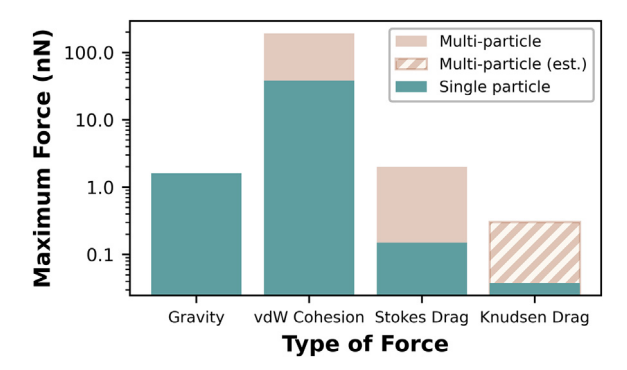


**Fig. 1.** Approximate maximum forces due to gravity, van der Waals cohesion, Stokes drag or Knudsen drag (for Kn = 1). Details on these calculations can be found in Appendix A.

velocities seen in CVR-ALD, we expect a pure DEM approach to accurately simulate the powder bed dynamics. By removing the fluid phase in this work, we can isolate solids-only interactions like vibration induced liftoff without the confounding effects of drag.

DEM takes the soft-sphere approach, where overlap is directly calculated for each collision, to resolve the contact forces. Soft-sphere contact models use a network of springs and dashpots normal and tangential to the point of contact to approximate the contact mechanics. A slider in the tangential direction accounts for finite Coulomb friction. The linear spring-dashpot model (LSD) was chosen as the soft-sphere contact model in this study. In the LSD model, the normal (subscript N) and tangential (subscript T) contact forces are given by

$$\bar{F}_{C,N}^{i,j} = -k_N \delta_N \hat{u}_N^{i,j} - \eta_N \frac{d\delta_N}{dt} \hat{u}_N^{i,j} \tag{3}$$

where k is the spring constant;  $\eta$  the dashpot coefficient;  $\delta$  the overlap for pair  $i,j;\mu$  the sliding (kinetic) friction coefficient; and  $\widehat{u}_N^{i,j}$  and  $\widehat{u}_N^{i,j}$  the unit vectors along and perpendicular to the i,j line of contact, respectively. The normal dashpot coefficient  $\eta_N$  is related to the normal coefficient of restitution  $e_N$  by

$$\eta_N = \frac{2\sqrt{k_N m_{eff}} |\ln e_N|}{\sqrt{\pi^2 + \ln^2 e_N}} \tag{5}$$

where  $m_{eff}=\frac{m_i m_j}{m_i+m_j}$  is the effective mass of the i,j pair. The relationships between tangential and normal spring constants  $\binom{k_7/k_N}{k_N}$  and dashpot coefficients  $\binom{n_7/n_N}{n_N}$  are typically set to a constant value of  $\binom{2}{7}$  and  $\binom{1}{2}$  in the linear spring-dashpot model, respectively.

The van der Waals cohesive force  $\sum_{k} \vec{F}_{vdW}^{i,k}$  is determined using the

Rumpf adhesion model. This model accounts for surface roughness through asperity height and requires fewer inputs than more complex expressions like the Rabinovich model [47].

$$\vec{F}_{vdW}^{i,k} = \frac{AR_{ave}}{12s^2} \left( \frac{r_i}{r_i + R_{ave}} + \frac{1}{\left(1 + \frac{r_i}{s}\right)^2} \right) \hat{u}_N^{i,j} \tag{6}$$

Here, A represents the Hamaker coefficient,  $R_{ave} = 2R_iR_j/(R_i + R_j)$  the average particle radius, s the separation distance of the adhesive pair, and  $r_i$  the asperity height. To avoid an infinite adhesive force at zero separation, an inner cutoff value is chosen equal to the typical minimum intermolecular distance (0.3 nm).

## 2.2. Simulation Setup

For particle flow modeling, we chose the widely used open-source code MFIX [48]. This multiphase flow package features many gas-solid flow modeling frameworks, a flexible graphical user interface, and easy implementation of user-defined functions. The discrete element method (MFIX-DEM) allows for easy particle tracking and explicit treatment of material properties such as friction coefficient and particle-particle stiffness. Simulations were performed using distributed memory parallelization on the RMACC Summit supercomputing cluster at the University of Colorado [49].

The breadth of relevant scales and the dynamic reactor motion present significant modeling challenges. The  $1200 \times 13 \times 45$  mm particle flow channel in a CVR-ALD system holds billions of 50 µm particles under typical operating conditions, near the practical upper limit for modern supercomputer calculations [50]. The simulation domain size must be reduced to avoid computationally expensive DEM simulations. Because we are working with light powder beds, where the conveyed mass is small relative to the conveyor mass and thus does not significantly influence the reactor's trajectory, we moved the conveyor kinematically using accelerometer data. This approach allows us to shrink our simulation size by using a periodic box model, providing flexibility in computational expense. The reactor kinematics can be incorporated as a position, velocity, or acceleration condition in a periodic box model. A hybrid condition with a fluctuating wall Y-velocity and fluctuating gravitational acceleration [51] was chosen for highest accuracy without the complexity of programming a moving mesh. These modifications were implemented using Fortran user-defined subroutines in the MFIX source code.

Soda-lime glass microspheres (GL0191B4, 45-63 µm) from Mo-Sci Corporation were chosen as the substrate material in this study (Fig. 2). These microspheres are an ideal material due to their wellcharacterized properties [52,53] and predictable flow behavior as mildly cohesive Geldart A powder. Ultrafine Geldart C powders (<20 µm) are also used as substrates in CVR-ALD but present a much higher computational expense in DEM and additional interparticle forces such as hydrogen bridging [54], wet cohesion, and electrostatic charging [55] become non-negligible at these small sizes. The particle-particle (P-P) Hamaker constant  $A_{pp}$ , the P–P friction coefficient  $\mu_{pp}$  and the P–P restitution coefficient  $e_{pp}$  were chosen based on experimental measurements for soda lime glass spheres [52,56]. An asperity height of 1 nm was selected to match experimental observations of pull-off force for 50 µm soda lime glass microspheres [53]. The particle-wall (P-W) Hamaker constant is calculated as the geometric mean from the interacting materials,  $A_{pw}$  $= (A_p A_w)^{1/2}$  [57]. Other material properties relevant to P-W interactions were taken from manufacturer data sheets or literature [52,56,58–61] (Table 1). The dimensionless granular P–P Bond number

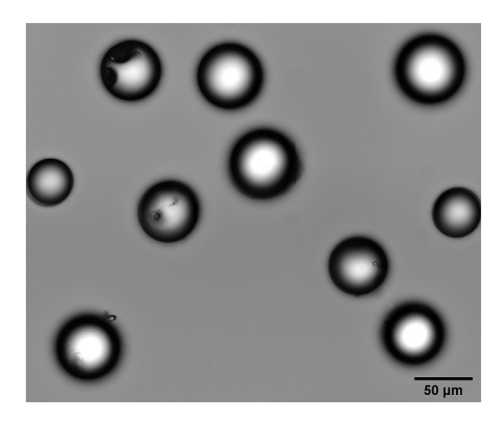


Fig. 2. Optical microscope image of 45–63 µm soda lime glass microspheres.

 $(Bo_{pp}^*)$  is also included in Table 1 to quantify the intensity of cohesive forces for 50  $\mu$ m soda lime glass spheres.

#### 2.3. Experimental Setup

Experiments were conducted using an in-house continuous vibrating bed reactor. (Forge Nano Inc., Colorado, Fig. 3). A pair of fiberglass leaf springs support the stainless steel reactor housing vibrated by a pneumatic linear actuator (Martin NTK 25 AL). Particles travel through the reactor on top of a 1/16" thick sintered stainless frit from Mott Corporation with a mean pore size of 10 µm to allow for purge gas and precursor gas flow during ALD. The gas flow was turned off ( $\nu_{\rm g}=0$ ) for all experiments in this work. Oscillation frequency and amplitude can be controlled independently by adjusting the supplied air pressure and the outlet metering valve position (SMC ASN2-03) to the pneumatic actuator, respectively. A Mide Slam Stick X tri-axial piezoelectric accelerometer (±16 g DC response MEMS, 1600 Hz sampling rate) was attached to the top of the reactor to measure conveyor acceleration. Powder convection velocity was determined by timing the powder's travel between two lines on the reactor with a stopwatch. Flow tests were performed at atmospheric pressure (626 Torr) and low pressure (2 Torr) using a vacuum pump. A camera mounted on a tripod captured top-view and side-view videos of powder flow behavior. The stainless upper chamber of the reactor was replaced with a transparent acrylic chamber during imaging tests. Stainless steel shim tape was placed over the inner walls of the acrylic to mimic the stainless walls of the upper reactor chamber.

A continuous function describing the reactor oscillations can be developed by reconstructing the accelerometer signal using the three largest-amplitude harmonics from Fast Fourier Transform decomposition (the "FFT model"). By summing the cosine waves of each  $m^{th}$  component with frequency  $f_m$ , phase angle  $\phi_m$ , and amplitude  $A_m$ , the FFT model for acceleration  $\ddot{x}$  in the  $k^{th}$  direction can be described by the equation

$$\ddot{x}_k(t) = \sum_m A_m \cos(2\pi f_m t - \phi_m) \tag{7}$$

This method requires a well-conditioned input data set with  $2^n$  data points, where n is any integer, for accurate amplitude and phase angle extraction. One challenge hindering accurate amplitude extraction is the slight irregularity in accelerometer sampling interval. Time step irregularities were corrected by resampling at a constant interval. Some amplitude loss was encountered during FFT signal decomposition, so

**Table 1**Properties used in DEM simulations to simulate Mo-Sci glass microspheres on a porous stainless surface.

Parameter	Value
Mechanical properties	
Particle diameter, $d_p$	50 μm
Particle density, $\rho_p$	$2500 \ kg/m^3$
P–P friction coefficient, $\mu_{pp}$	0.273
P–W friction coefficient, $\mu_{pw}$	0.4
P–P restitution coefficient, $e_{pp}$	0.97
P–W restitution coefficient, $e_{pw}$	0.83
Particle Young's modulus, $E_p$	73 GPa
Wall Young's modulus, $E_w$	22 GPa
Particle Poison's ratio, $\nu_p$	0.22
Wall Poison's ratio, $ u_w$	0.07
Cohesive properties	
P–P Hamaker constant, App	$3.1 \times 10^{-20} J$
P-W Hamaker constant, A <sub>pw</sub>	$6.2 \times 10^{-20} J$
Asperities	1 nm
Outer cutoff (for $F_{van \ der \ Waals}$ )	10 nm
Inner cutoff (for $F_{van \ der \ Waals}$ )	0.3 nm
$Bo_{pp}^* = F_{cohesion/m_pg}^{max}$	24

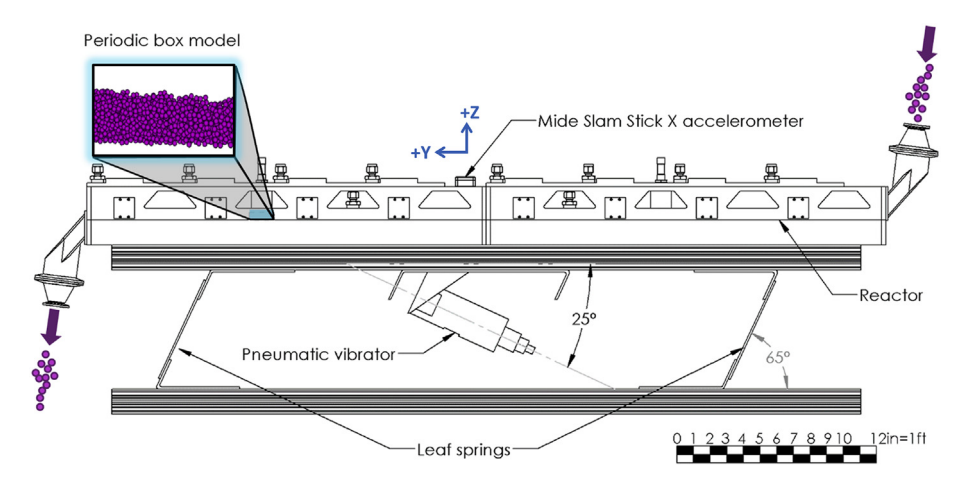


Fig. 3. Computer-aided design (CAD) model of the continuous vibrating bed reactor. CAD models of the pneumatic vibrator and accelerometer were obtained from GrabCAD. Exploded inset provides context for the approximate region simulated by the periodic box model.

the FFT model amplitude was magnified slightly through multiplication by a constant "mod factor" based on the maximum amplitude of the low pass filtered signal. Finally, a numerical fitting procedure was applied to the phase angles, which are not well determined from FFT, using MATLAB's *fmincon* function. With an FFT model in place, the signal is integrated once to determine velocity  $\dot{x}_k$  and twice to determine position  $x_k$  as described by

$$\dot{x}_k(t) = \sum_m \frac{A_m}{2\pi f_m} \sin(2\pi f_m t - \phi_m)$$
 (8)

$$x_k(t) = \sum_{m} \frac{-A_m}{(2\pi f_m)^2} \cos(2\pi f_m t - \phi_m)$$
 (9)

## 3. Results and Discussion

# 3.1. Characterizing Vibratory Convection

We need frequency and amplitude data to describe the reactor vibration as inputs to the vibrating bed DEM simulation. Y and Z-acceleration data (Fig. 4A, C) were obtained for an inlet pressure of 60

psi at maximum amplitude (100% open throttle) and used as the baseline case. A Fast Fourier Transform was performed on the Y/Z-acceleration in MATLAB using the built in fft function to reveal the underlying frequencies (Fig. 4B, D). For the purposes of this discussion, the +Y axis lies along the primary flow direction (reactor long axis) and -Z axis lines up with gravitational acceleration (Fig. 3). X acceleration was disregarded as noise and omitted due to X-direction constraints by the reactor walls and lack of X-motion observed experimentally. Accelerations are normalized by Earth's gravity through the acceleration ratio  $\ddot{x}_k/g$ . A conveyor acceleration equal to gravity,  $\ddot{x}_k = 9.81 \ m/s^2$ , corresponds to a normalized "g-force" of 1 g.

Both the principal (Y) and gravity (Z) directions are characterized by high-g total acceleration. Despite strong differences in high-frequency content, both directions have similar acceleration amplitudes at low frequencies. The dominant frequency in the FFT results matches the base actuator frequency of 48 Hz, so although reactor displacement is only submillimeter, maximum accelerations are >1 g in both Y and Z-directions. Another interesting feature is the strong presence of integer multiples of the fundamental frequency, also called "harmonics". Both directions have strong harmonics, but the Z direction shows significantly stronger resonance than the Y direction. The bolts holding the top and bottom halves of the assembly together may be acting as

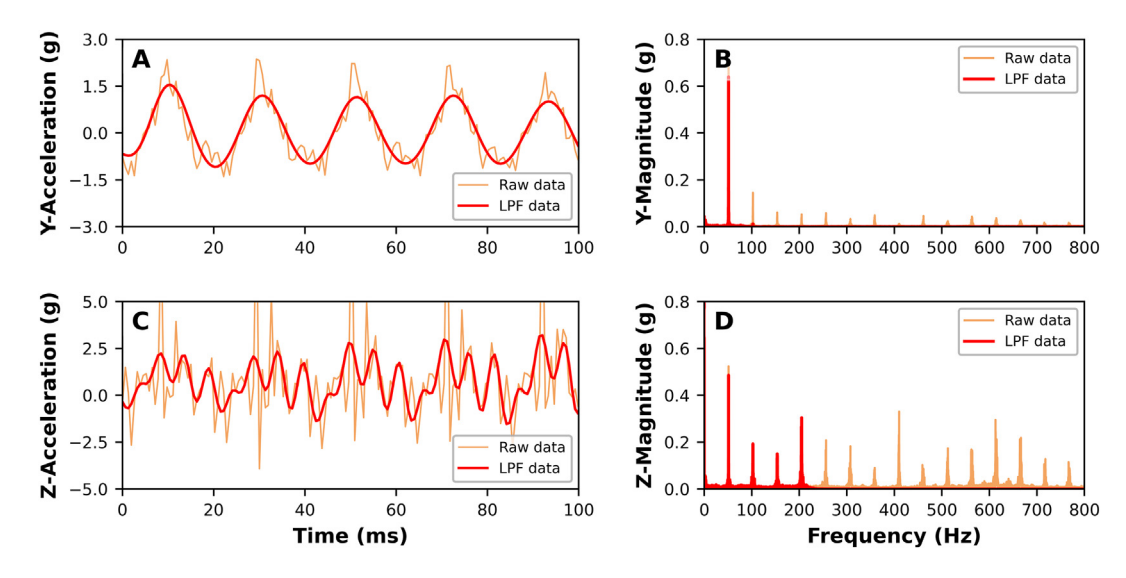
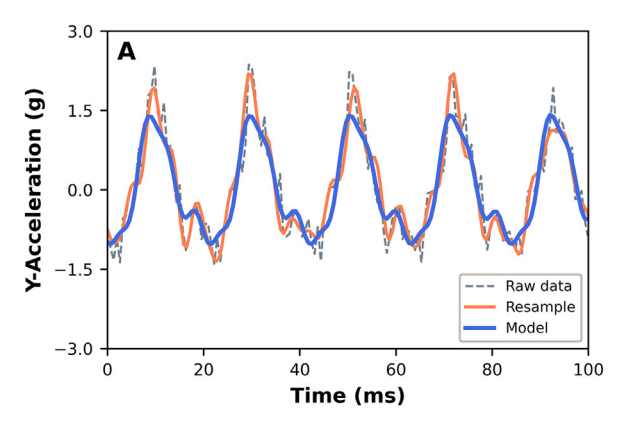
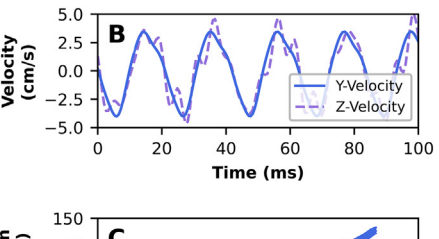


Fig. 4. Plots of raw time-domain (A, C) and frequency-domain (B, D) accelerometer results. Low-pass filtered ("LPF") data are overlaid to emphasize the relative magnitude of low-frequency components.





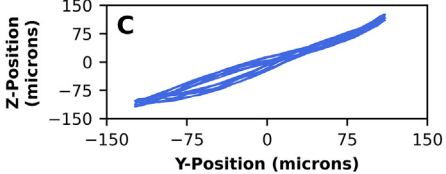


Fig. 5. (A) Raw accelerometer data with resampled waveform and FFT model overlaid. Velocity (B) and position (C) were determined by integrating the FFT acceleration model.

nodes along the reactor body, allowing small standing waves to form between anchor points in the unconstrained Z-direction. The resonance behavior of steel, which makes up most of the reactor body, has been correlated with microstructural properties such as alloy composition, material hardness, fracture toughness, and the presence of nonmetallic inclusions [62,63]. Rigidity and composition of the support can be tuned to produce the desired harmonic response, enabling harmonic intensity to be treated as a degree of freedom. The influence of resonance on powder flow behavior is investigated further in Section 3.3. Details on the waveform characteristics (amplitude, frequency, and phase for Fig. 5 data) can be found in Table 2.

The presence of frequency  $f_m$  in the coefficient denominators causes high-frequency components to drop out upon integration, so Y and Zposition are similar even though Y and Z-acceleration are not. The Y and Z-positions form two in-phase sinusoids of similar magnitude, consistent with the "forward and upward" extension and "backward and downward" retraction mechanism. Under these conditions, many modes of motion are available to the particles, including no-slip conveyor contacting, forward sliding, backward sliding and hopping [64]. There are two mechanisms that could explain the bulk convection of powder in a CVR-ALD reactor. Mechanism 1 is a no-slip/slip mechanism or "continuous contact" conveying and is common for non-sinusoidal conveyors [65]. Continuous contacting assumes the particles maintain some contact with the conveyor during extension but slide on the conveyor during retraction, giving net-forward motion. Mechanism 2 is a throw or hopping mechanism, the most common method discussed in literature [64]. Here, the particles once again maintain contact with the conveyor during extension but then lose contact or "lift off" from the conveyor during retraction, producing net-forward motion. In addition to conveyor design and operating conditions, we expect that particle properties such as friction coefficient, Hamaker constant, and coefficient of restitution will determine which convection mechanism dominates. To the authors' knowledge, there has been no investigation into the possibility of a hybrid slide-throw mechanism. For certain fine powders with low P-W friction or excited by high Y-acceleration, the bed may convey in a hybrid state, where some micro-slipping occurs for bottom-layer particles at the conveyor-particle interface and some liftoff occurs in the powder bulk during frit retraction. The cutoff between hopping and sliding is difficult to distinguish experimentally,

**Table 2**Sample waveform characteristics from FFT model fitting.

	1Y	1Z	2Z	3Z
Amplitude, $A_m$ $[m/s^2]$	10.581	10.273	10.114	9.154
Frequency, $f_m$ [Hz]	48	48	192	167
Phase, $\phi_m$ [rad]	3.08	3.08	-2.66	-1.38

but we can investigate the contact behavior at the particle-wall interface under vibratory convection through DEM simulations.

## 3.2. Modeling Particle Convection With DEM

Simulations were run using the conditions defined in Table 3. A detailed explanation for these simulation parameters can be found in Appendix B. To aid in discussion of the results, we will define several theoretical limits for powder convection based on the reactor kinematics and idealized hopping trajectories (Fig. 6). First, we will use the "straight drop" solution to define a lower limit on ideal convection. This trajectory assumes that the particle travels with the conveyor on the extension stroke and separates or "lifts off" at the start of the retraction stroke. In this case, the conveyor imparts the minimum forward velocity possible (zero) to the particle during the flight stage, leading to no forward motion during the retraction stage and a time-averaged con-

vection velocity of  $\frac{\binom{n_1}{2\pi r_1^2}}{T} = \frac{226 \ \mu m}{20.83 \ ms} = 1.08 \ cm/s$ . At the other extreme, we have the "perfect flight" solution, where particles travel at the maximum conveyor velocity of 3.51 cm/s and only briefly contact the frit before being launched again. It is worth noting that perfect flight conditions, which correspond to vibro-fluidization, typically require high conveyor accelerations >3 g [66]. This speed can also be theoretically achieved through a slip/slip 'sealskin' convection mechanism if the particles slide forward on a frit material with a high extension friction coefficient and low retraction friction coefficient [67]. The true velocity profile of the powder bed will depend on the particle-particle and particle-wall dynamics which determine exactly when liftoff or sliding occurs. Here, any real convection velocity between the perfect flight and straight drop solutions will be referred to as "ideal" convection, and any below the straight drop solution as "partial" convection. Neither straight drop nor perfect flight are fully achievable in practice but can still be used to benchmark conveying efficiency.

The simulated powder velocity profile includes features of the straight drop and perfect flight limiting behaviors. As in the straight drop approximation, the powder follows a quasi-sinusoidal forward trajectory during frit extension but lifts off before the extension stroke is complete. The point when liftoff begins varies from cycle to cycle but

**Table 3**Simulation geometry and parameters.

Parameter	Value
Periodic box depth Periodic box width Static bed height Simulated P-P spring constant, kpp	0.25 mm/5d <sub>p</sub> 5 mm/100d <sub>p</sub> 0.75 mm/15d <sub>p</sub> 2500 N/m
Simulated P–W spring constant, $k_{pw}$	1562.5 N/m

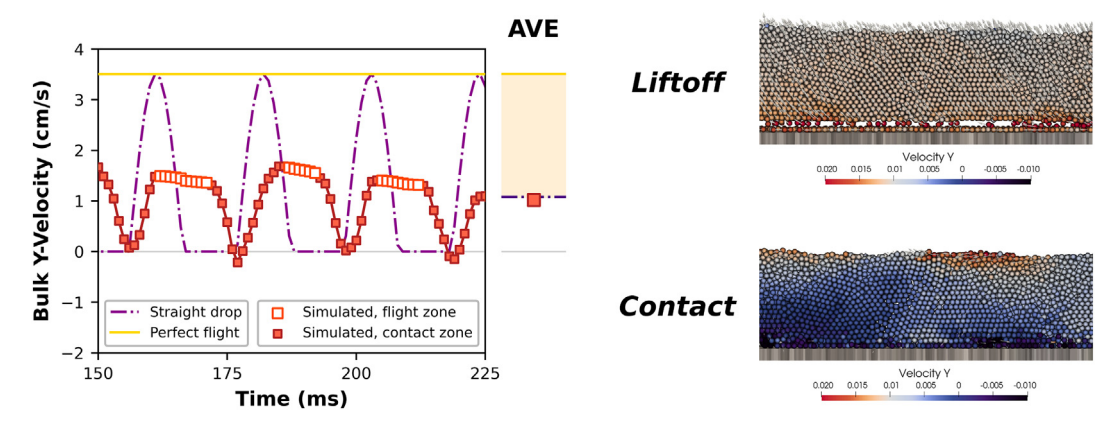
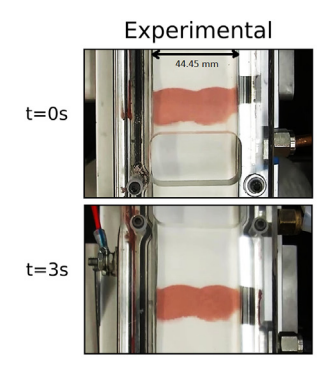


Fig. 6. Simulated powder convection velocity compared to limiting behavior under straight drop and perfect flight conditions. Time average for the simulated profile (square point) relative to the time averages from the analytical solutions (straight and dash-dot lines) is displayed in AVE. Yellow shading spans the range of time-averaged velocities corresponding to ideal convection.

is typically near the middle of the extension stroke, at maximum frit velocity. During liftoff, the particles travel under free flight as indicated by the plateau in convection velocity. This trajectory is analogous to the constant horizontal velocity imparted on a projectile in the absence of drag. The particles then recontact the frit around the middle of the retraction stroke and undergo a deceleration period before establishing no-slip contact with the frit. A lack of particle-wall sliding in the simulations indicates that a pure hopping mechanism, not a hybrid sliding-hopping mechanism, is dominant for 50 µm glass microspheres under ~1 g excitation.

Qualitatively, both the simulated and experimental results show nearly ideal plug flow behavior (Fig. 7 and Supplementary Videos S1 and S2). Individual microspheres are difficult to distinguish during reactor vibration, so a row of microspheres was colored with Jacquard Piñata Color glass dye to track particle movement during the stopwatch tests. Simulated particles were also colored to aid in side-by-side comparisons with the tracer tests from the experimental setup. Side views of the simulation results show a clear front of particles with nearly uniform powder velocities in the bulk and lower, nonzero convection velocities at the particle-frit interface. Dispersion can be observed in the bottom particle layer due to cohesive particle-frit interactions impeding forward convection. Top views from both the experimental and simulated results show smooth, consistent fronts of tracer particles. Significant changes in particle-wall stickiness or friction, which can occur with a new substrate material or deposited film chemistry, will likely affect the shape of this convection profile. It is also worth noting that the periodic box model, by virtue of being periodic, assumes reactor-depth-independent flow behavior. Here, where wall-to-wall deviations from ideal plug flow are relatively small, the periodicity approach was able to produce realistic results. Powders other than soda lime glass may not exhibit ideal plug flow experimentally, so the validity of a periodic box for vibrating bed reactor modeling should be verified on a case-by-case basis.

Differences in mean convection velocity between ambient pressure and low-pressure tests indicate that drag effects play a role in the low Knudsen number regime at all three actuator conditions tested (Fig. 7). Even a stationary background gas phase would lead to noticeable Stokes drag in a porous vibratory conveyor, where maximum reactor Z-velocities are comparable to the minimum fluidization velocity of the powder. The low-pressure condition shows closer agreement to the DEM results than tests at ambient pressure. At room temperature and 2 Torr, the mean free path of nitrogen molecules is around 25 µm, half of the mean particle diameter. Dense, highly coordinated particle regions further confine the gas flow to small interstitial spaces between particles. Slip-flow or free molecular flow may be occurring in the interstitial gaps, reducing the effective drag force and leading to improved agreement between experimental and simulated results at low pressure. The remaining disagreement between experimental and simulated results at 2 Torr may also be due to imperfect determination of the frit excitation amplitude. All assemblies have finite rigidities and measured acceleration is known to vary with accelerometer placement [68]. The channel containing the thin reactor frit, which is too shallow for accelerometer placement, may be experiencing higher accelerations than the thick and rigid reactor upper chamber where the accelerometer is mounted. The accelerometer sensor's signal-to-noise ratio and the FFT



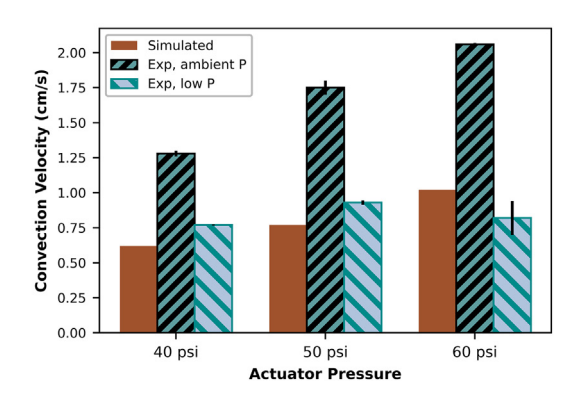
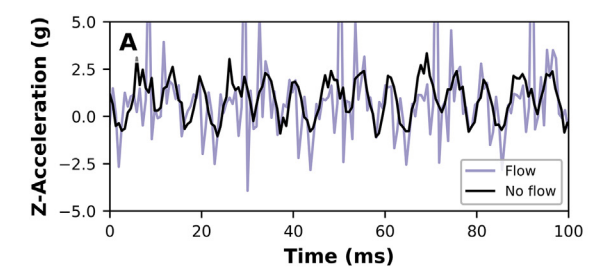


Fig. 7. Snapshots from experimental tracer tests at two different points in time illustrating the solids flow behavior. Time-averaged convection velocity from the simulations is compared to the experimentally determined convection velocities at ambient pressure (626 Torr) and low pressure (2 Torr). Errors bars represent the calculated standard deviation from 3 replicates at each actuator pressure.



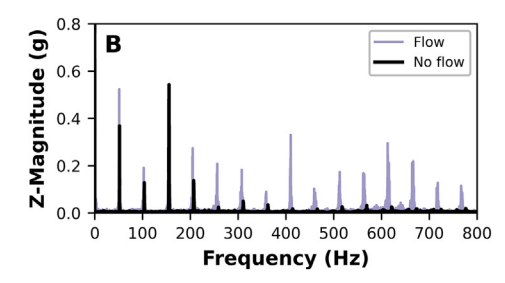


Fig. 8. Raw time-domain (A) and frequency-domain (B) acceleration data when powder "flow" and powder "no flow" was observed.

signal decomposition process also have finite resolutions that limit their accuracy. Jump discontinuities in the accelerometer data lead to ringing artifacts such as Gibbs phenomenon during signal processing [69]. Further studies will be needed to explore gas-phase effects in the low Knudsen number regime.

## 3.3. The Role of High-Frequency Excitation

The rigidity of the reactor support plays a role in the solids flow behavior through amplification or attenuation of conveyor resonance. To illustrate this, accelerometer results (Fig. 8) are provided for two different conveyor support structures at the same actuator conditions (60 psi, 100% open throttle). The "no flow" conveyor support had a smaller leaf spring separation and less rigid base than the improved "flow" conveyor support structure from Fig. 3. There are two noticeable changes from the no flow to the flow scenario. The first is an increase in the amplitude of the first harmonic. The second is the magnification of higher resonant frequencies. Resonance caused by operating frequencies near the conveyor's natural frequency are hazardous, generating dangerously large deflections and high stresses that compromise mechanical integrity of the entire structure [70]. However, low amplitude resonance of individual components such as the frit may improve powder agitation and flow. Conveyor resonance characteristics are a key component in resonance-based vibratory feeders but often ignored in brute force driving mechanisms like the pneumatic actuator in this study. Either, or both, of these factors could explain the transition to steady powder flow. Although the beneficial effects of increasing the first harmonic amplitude have been documented for low-g conveyors [15], the superposition of resonant frequencies and their effects on powder flow behavior in brute force vibratory convection remain unreported.

To support the notion that resonant frequencies play a role in hopping convection, FFT models are presented at near-1 g conditions (Fig. 9). Shading corresponds to favorable periods for liftoff when the net force due to gravity and vibration is <0 g and results in momentary particle weightlessness. The importance of weightlessness in hopping convection has been discussed by other researchers in the vibratory conveying field [15]. Considering only the first harmonic ("1f" in Fig. 9), a < 1 g case will always remain above the 0 g threshold. Ensuring

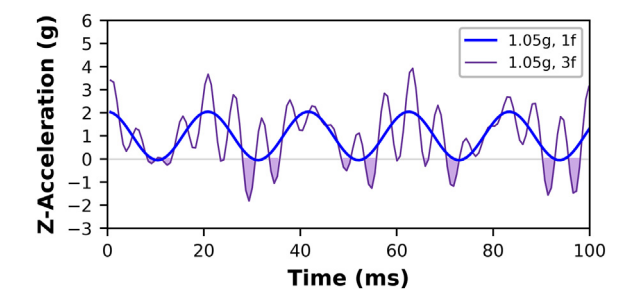


Fig. 9. FFT model acceleration with regions  $< 0~{\rm g}$  shaded to highlight instances of weightlessness.

hopping convection of bottom layer particles impeded by downward-acting contact forces will require a net force due to vibration and gravity <0 g. A first harmonic of 1.05 g (Table 2) leads to some instances of weightlessness, but they are small and short-lived. After incorporating the two strongest resonant frequencies ("3f"), the number and magnitude of weightlessness instances greatly increases. This increase in <0 g occurrences with resonance can be seen in the raw accelerometer data between the no flow and flow cases (Fig. 8). Thus, Z resonance can be considered a tunable parameter to increase the duration of <0 g events without changing Y acceleration.

# 3.4. Optimizing Convection Efficiency

Another implication of this frequency sensitivity is the opportunity for optimizing the excitation waveform. Alternatives to the simple sinusoidal waveform, from out-of-phase sinusoids [71] to non-sinusoidal excitation [27,65], provide another avenue for improving powder flow behavior in vibratory convection. Excitation modifications may be needed in cases where increasing total acceleration amplitude to drive powder flow comes with undesirable side effects. Y and Z are geometrically linked by the leaf spring setup such that we cannot independently vary the Y and Z excitations without making support modifications. This geometric constraint limits the minimum steady powder convection velocity that can be achieved under hopping convection in a horizontal conveyor, which requires >0.5 g Z accelerations [64]. Lower convection velocities corresponding to <0.5 g in the Y direction may be desirable in CVR-ALD for ultrafine powders that easily elutriate at >1 g or slow chemistries that require longer dose times. Changes to the vibration waveform or superposition of resonant frequencies by using stiffer metal support structures, which introduces randomness to the agitation, may be more effective at separating cohesive particle-wall contacts and promoting steady powder flow than increasing the first harmonic amplitude.

We will investigate an excitation waveform that enables lower convection velocities of highly cohesive fine powders in CVR-ALD. In both the continuous contact and hopping mechanisms, we want to optimize particle translation during extension. Lower speeds on the extension stroke should decrease particle backward slipping during convection. To discourage sticking during retraction, which reverses forward progress made during the extension stroke, higher retraction speeds are desired. Here, we propose a reactor position profile that follows a sawtooth waveform to minimize extension-backsliding and retraction-sticking tendencies.

To approximate a sawtooth, we use a piecewise sinusoid with low-frequency extension and high-frequency retraction (Fig. S1). The maximum displacement of this pseudo-saw is set equal to the baseline sinusoid (113  $\mu$ m) for comparison purposes, so that the lower velocity limits as defined by straight drop convection are the same. The piecewise function is defined using relative time  $t^* = mod(t/T_1)$  with respect to the period of the baseline sinusoid  $T_1$ . The constraints for a continuous piecewise sinusoid with the same amplitude and total period as the baseline sinusoid are

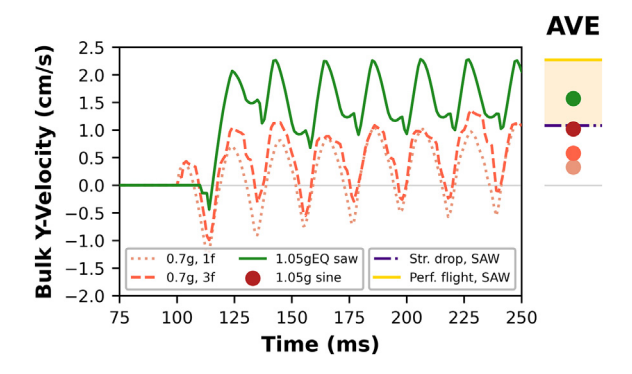


**Fig. 10.** Spatially averaged powder y-velocity for the baseline case from Fig. 6 (1.05 g sine) versus low-amplitude cases (0.7 g, 1f and 0.7 g, 3f) and optimized sawtooth waveform with an "effective" average acceleration equal to the baseline case (1.05gEQ saw). Time average for the simulated sawtooth profile is compared to averages for the simulated sine waves (AVE).

$$\frac{1}{f_a} + \frac{1}{f_b} = \frac{2}{f_1} \tag{10}$$

$$\sin{(2\pi f_a t_{crit} - \phi_1)} = \sin{(2\pi f_b t_{crit} - \phi_b)} \ \ \textit{where} \ t_{crit} = \frac{1}{4f_a} + \frac{\phi_1}{2\pi f_a} \ (11)$$

where  $t_{crit}$  refers to the transition point between half sines a and b, when the first half sine is at its maximum. For simplicity, we have chosen  $f_a = 2/3 f_1$  in this study.  $\phi_b$  is solved for numerically using the constraint defined in Eq. 11. Combining these relationships results in a piecewise function as described by Eq. 12.

$$x(t^{*}) = \begin{cases} \frac{A_{1}}{(2\pi f_{1})^{2}} \sin(2\pi f_{a}t^{*} - \phi_{1}), \ t^{*} < t_{crit} \\ \frac{A_{1}}{(2\pi f_{1})^{2}} \sin(2\pi f_{b}t^{*} - \phi_{b}), \ otherwise \end{cases}$$
(12)

The pseudo-saw waveform results in higher convection velocities than the sinusoidal waveform (Fig. 10). Although the pseudo-saw travels slower on extension, giving a lower perfect flight maximum of 2.27 cm/s than the baseline sine from Fig. 6, the hopping convection cycle is more effective, giving a higher time-averaged velocity of 1.57 cm/s. Particles under this excitation remain in liftoff during the full retraction phase, avoiding the low or even backwards velocities observed under pure sinusoidal excitation.

Simulations incorporating higher resonant frequencies were also performed to verify the role of resonance proposed in Section 3.3. As expected, the time-averaged convection velocity increased from 0.33 to 0.58 cm/s when the next two resonant frequencies were added to a bed excited at 0.7 g (Fig. 10). Liftoff plateaus appeared once higher frequency content was included, indicating an improvement in convection behavior. Smaller dips in the bulk velocity profile also demonstrate a decrease in backflow for the three-frequency case. Higher amplitude excitations (>0.9 g) at the same fundamental frequency showed little to no change when additional frequencies were incorporated, indicating that resonance improves convection through promotion of weightlessness when the first harmonic is <1 g. Thus, high-frequency Z resonance contributes to achieving the weightlessness necessary for powder liftoff in sub-1 g conveyors.

The robustness of the pseudo-saw waveform is best demonstrated with a highly cohesive substrate. Large Hamaker coefficients of  $A_{pp} = A_{pw} = 4 \times 10^{-19} J$  were used to describe a highly cohesive powder, increasing the  $Bo_{pp}^*$  number from 24 to 307. Hamaker constants or  $Bo_{pp}^*$  numbers of this magnitude can be expected among metallic substrates [57] or particles in high humidity environments based on pull-off force measurements [72] and have been used by other researchers

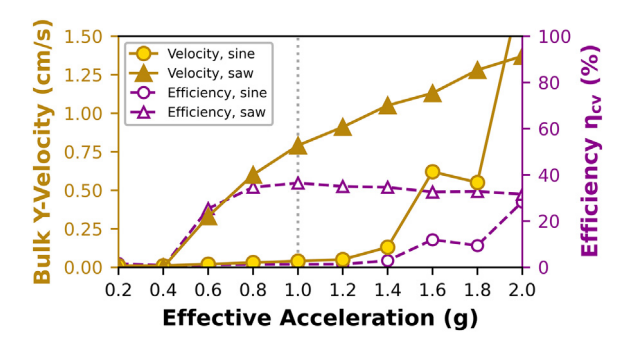


Fig. 11. Convection velocity and efficiency comparisons for the sawtooth and sinusoidal waveforms.

to simulate micron-size cohesive powders [73]. Effective acceleration for the sawtooth waveform, which has a piecewise varying acceleration, refers to acceleration based on the displacement equalization procedure described in Eqs. 11 and 12. A regular basis must be defined for comparisons since the sawtooth waveform has a lower maximum extension velocity at each effective acceleration than the sinusoidal waveform. Here, we normalize the results by defining a convection velocity efficiency  $\eta_{cv}$  based on the time-averaged simulated particle velocity  $v_{p,ave}$  and maximum frit extension velocity  $v_{w,max}$ :

$$\eta_{cv} = \frac{|v_{p,ave}|}{|v_{w,max}|} \tag{13}$$

As expected, the sawtooth waveform produces higher convection velocities and more consistent convection efficiencies than the sinusoidal waveform at sub-2 g input accelerations (Fig. 11). The sinusoidal waveform is unable to produce consistent and measurable powder convection until >1.4 g acceleration, indicating a failure to break cohesive particle-wall bonds during frit retraction. The 1.4 to 2 g input region is also marked by severe fluctuations in bulk velocity and hopping suppression. Consistent powder flow behavior is not observed until at least 2.2 g, when the sinusoidal waveform stabilizes at around 38% convection efficiency. The 2.2 g cutoff corresponds to a minimum convection velocity of 2.84 cm/s that can be reliably achieved with this sinusoidal excitation, higher than the <2 cm/s velocities ideal for adequate precursor exposure in typical CVR-ALD reactors. By contrast, the sawtooth waveform demonstrates stable powder convection for velocities as low as 0.33 cm/s with clear and consistent liftoff regions for all accelerations >0.4 g and stable convection efficiencies around 34% for >0.8 g accelerations. When cohesive particle-wall interactions prevent powder convection, sinusoidal excitation can be replaced with an optimized sawtooth waveform to achieve slow, steady powder flow.

## 4. Conclusions

The solids flow behavior of fine cohesive powder in a vibrating bed reactor was studied using the discrete element method. Bulk simulated velocity results revealed clear liftoff plateaus typical of a hopping convection mechanism. In experimental and simulated tracer tests, the powder bed exhibited nearly ideal plug flow behavior. For the pure DEM approach taken in this work, close agreement between experiments and simulations can only be expected in the high Knudsen number regime where gas-particle drag is negligible. With gas manifolds turned off, particles moving through a quiescent background gas phase at ambient pressure travel at conveyor velocities close to the minimum fluidization of fine Geldart A powders, generating appreciable drag forces. Tests at high and low reactor pressures corresponding to particle Knudsen numbers in the continuum and slip-flow regimes, respectively, confirmed that only the low-pressure case achieved

quantitative and qualitative results that were comparable with the experimentally observed solids flow behavior.

FFT decomposition of the reactor acceleration revealed the importance of high-frequency excitation for horizontal conveyors at low-g accelerations. Adjustments to the excitation waveform or the resonance behavior provide another avenue for improving powder flow behavior. Flow improvements under the novel sawtooth waveform demonstrate the importance of high-g retraction for convection of highly cohesive fine powders at low flow velocities. If steady powder flow is not possible under simple sinusoidal excitation, the waveform can be optimized by tuning half-wave frequency and amplitude. Future work will incorporate the gas phase in a CFD-DEM model for investigations into the gas-solid coupling and its effects on flow behavior.

# Appendix A. Supplementary data

Supplementary data to this article can be found online at https://doi.org/10.1016/j.powtec.2021.03.038.

## **Declaration of Competing Interest**

A.W. Weimer has a significant financial interest in Forge Nano.

#### Acknowledgements

The authors are grateful for the support of the National Science Foundation [NSF GOALI #1852824]. This work utilized the RMACC Summit supercomputer, which is supported by the National Science Foundation (awards ACI-1532235 and ACI-1532236), the University of Colorado Boulder, and Colorado State University. The Summit supercomputer is a joint effort of the University of Colorado Boulder and Colorado State University. The authors also thank Forge Nano for providing the CVR-ALD reactor and Jay Valuet at Martin Vibration Systems for helpful discussions and feedback on upgrading the vibratory convection setup.

## **Appendix A. Estimating Maximum Forces**

The maximum force estimates in Fig. 1 were determined using CVR-ALD reactor conditions and equations from literature. The cohesive force was calculated using Eq. 6 for a single contact (single-particle) and 5 contacts (multi-particle) at a minimum separation of 0.3 nm, a Hamaker constant of  $A=3.1\times10^{-20}J$  and an asperity radius of 1 nm. Drag forces were determined using the single-particle drag expression

$$F_{D} = \frac{1}{2} \rho_{g} (u_{p} - v_{g})^{2} C_{d} \frac{\pi}{4} d_{p}^{2}$$
 (A1)

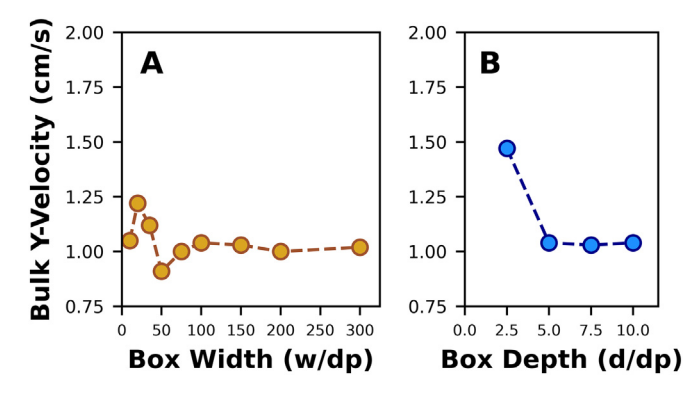


**Fig. B1.** (A,B) Sensitivity tests on periodic box size. Box dimensions are specified in terms of number of particle diameters.

where  $\rho_g$  is the gas density;  $u_p$  the particle velocity;  $v_g$  the gas velocity;  $C_d$  the drag coefficient; and  $d_p$  the particle diameter. A maximum relative velocity of ~2 cm/s was chosen for 50-µm soda lime glass microspheres based on minimum fluidization velocity and tested actuator conditions. Stokes drag  $\left(C_D = \frac{24}{Re}\right)$  was used in Fig. 1 due to the low characteristic Reynolds numbers  $\left(Re = \frac{\rho_g |u_p - v_g| d_p}{\mu_g} < 0.1\right)$  at CVR-ALD reactor conditions. For multi-particle drag, an estimate based on the Ergun drag coefficient correlation

$$C_D = \frac{a}{Re} \frac{1 - \varepsilon}{\varepsilon^2} + \frac{B}{\varepsilon^2} \tag{A2}$$

with a=180, b=1.8, and  $\varepsilon=0.50$  was used [74]. The single-particle Knudsen drag correction from Loth at Kn=1,

$$C_{D,Kn,Re} = \frac{\frac{24}{Re} \left( 1 + 0.15 \, Re^{0.637} \right)}{\left( 1 + \left( 2.514 + 0.8e^{\frac{-0.55}{Rn}} \right) Kn \right)} \tag{A3}$$

was used for the Knudsen estimate in Fig. 1 [75]. The presence of nearby particles is known to increase the drag force, and while multi-particle correlations for high-Knudsen aka "rarefied" flows are lacking in literature, an approximate magnification factor was applied in Fig. 1 using Lattice Boltzmann simulation data on multi-particle arrays in boundary-slip flows at low Re [76]. The chosen magnification factor (8) is likely an overestimate for Kn=1 and thus a conservative guess for maximum multi-particle Knudsen drag. As the Knudsen number increases (i.e. lower reactor pressures) the relative influence of drag will continue to decrease.

## **Appendix B. Choosing Appropriate Simulation Conditions**

The domain size and simulated P–P/P–W stiffness in a periodic box model must be chosen carefully. At a minimum, the periodic box must be large enough that further increases in the box size do not affect the simulation results. Domain sensitivity tests revealed the need for periodic box sizes  $\geq$ 75 particle diameters wide and  $\geq$ 5 particle diameters deep for system-size independent results based on trends in the spatially averaged ("bulk") powder velocity (Figs. B1A, B).

Simulations using a nonlinear (Hertzian) spring-dashpot model were performed to verify the accuracy of a linear spring-dashpot model for low-g vibratory convection. The Hertzian model is based on the linear theory of elasticity and is highly accurate for low-strain collisions of elastic spheres [77]. The linear spring-dashpot model provides a computationally efficient linearization to Hertzian contact mechanics and, for near-elastic behavior ( $e_{pp}>0.8$ ), has been shown to agree with experimental results fairly well [78]. Both models predict similar forces for collisions involving small deformations and low impact velocities. Since no prior DEM simulations have been performed on CVR-ALD, it was important to test the validity of the LSD model against the Hertzian results.

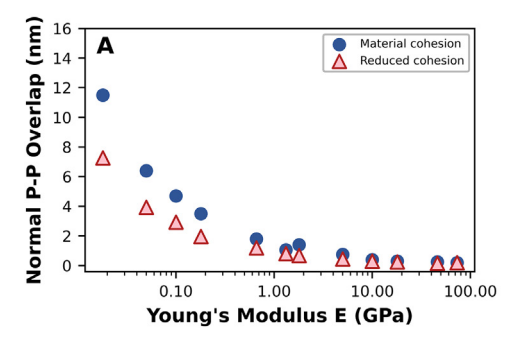
The Hertzian contact model utilizes a nonlinear relationship between overlap  $\delta$  and contact force as described by

$$\bar{F}_{C,N}^{i,j} = -\frac{4}{3} E_{eff} \sqrt{R_{eff}} \delta_N^{3/2} \hat{u}_N^{i,j} - \eta_N \frac{d\delta_N}{dt} \hat{u}_N^{i,j} \tag{B1} \label{eq:B1}$$

$$\bar{F}_{C,T}^{i,j} = \begin{cases} -\frac{16}{3} G_{eff} \sqrt{R_{eff}} \delta_N^{1/2} \delta_T \hat{u}_T^{i,j} - \eta_T \frac{d\delta_T}{dt} \hat{u}_T^{i,j}, \ |\bar{F}_{C,T}^{i,j}| < \mu |\bar{F}_{C,N}^{i,j}| \\ -\mu |\bar{F}_{C,N}^{i,j}| \hat{u}_T^{i,j}, \ otherwise \end{cases}$$
(B2)

In the Hertzian model, both the tangential and normal contact forces are dependent on normal overlap  $\delta_N$ , and the material properties of in-

terest are the effective Young's Modulus, 
$$E_{e\!f\!f} = \left(\frac{\left(1-\nu^{j^2}\right)}{E^l} + \frac{\left(1-\nu^{j^2}\right)}{E^l}\right)^{-1}$$



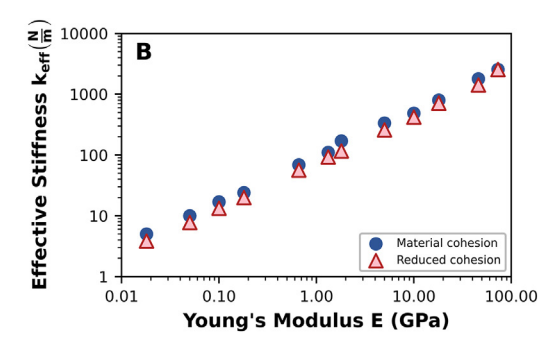
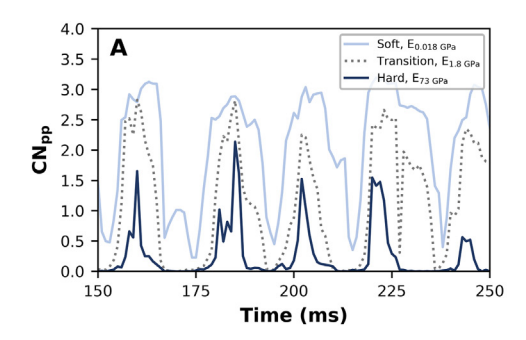


Fig. B2. (A) Relationship between time-averaged normal overlap and simulated Hertzian stiffness using a fixed material Hamaker constant versus a stiffness-scaled Hamaker constant ("reduced cohesion"). (B) Relationship between simulated stiffness in the Hertzian model (Young's modulus) and calculated stiffness for the LSD model (effective spring constant) with and without reduced cohesion.



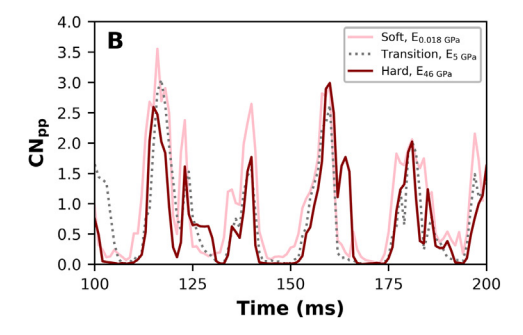


Fig. B3. Time evolution of spatially averaged particle-particle coordination number at different reduced spring stiffnesses without reduced cohesion (A) and with reduced cohesion (B).

and an effective Shear Modulus,  $G_{eff} = \frac{E_{eff}}{2+2\nu_{eff}}$ , for each i,j pair. The effective radius of the colliding pair,  $R_{eff} = \frac{R_i R_i}{R_i + R_j}$ , also plays a role in the resulting force. The normal damping coefficient  $\eta_N$  can be related to the normal coefficient of restitution  $e_N$  by the relationship

$$\eta_{N} = \frac{-2\sqrt{15}R_{eff}^{-1/4}\sqrt{m_{eff}E_{eff}}\ln e_{N}}{3\sqrt{\pi^{2} + \ln^{2}e_{N}}}\delta_{N}^{-1/4} \tag{B3}$$

Unlike in the LSD model, the Hertzian dashpot coefficient depends on normal overlap  $\delta_N$ . Typically, the tangential damping coefficient  $\eta_T$  is assumed equal to the normal damping coefficient  $\eta_N$  [79].

In the LSD model, material stiffness is described by the spring constant k. The Hertzian model uses Young's modulus E for stiffness. To make direct comparisons between both models, Hertzian stiffness can be recast as a linearized spring constant [80]  $k_{n,eff}$  through the equation

$$k_{\textit{n,eff}} = k_{\textit{n,Hertz}} \sqrt{\delta_{\textit{n}}} = \frac{4}{3} E_{\textit{eff}} \sqrt{r_{\textit{eff}} \delta_{\textit{n}}} \tag{B4}$$

Linearized spring constants based on collisional velocity [80,81] and/ or overlap [80] gave similar results of around 1000–4000 N/m for the material spring stiffness. Particle behavior was dominated by enduring, multiparticle contacts rather than binary collisions, so the value based on average overlap (2500 N/m) was chosen as the true linear spring stiffness in this study.

Reduced stiffnesses are often used to keep the computational expense low when modeling gas–solid systems. For cohesive particle modeling, care must be taken to avoid choosing an excessively reduced spring constant. Previous studies have shown that a reduced stiffness can artificially increase the area of contact and lead to overprediction of the cohesive force if an appropriate scaling law is not implemented [82,83]. Kobayashi et al. demonstrated the need for spring constants ≥1000 N/m to obtain fluidized bed bubbling patterns that match

experimental results for mildly-cohesive 60  $\mu$ m soda lime glass spheres [81]. When using reduced stiffnesses, a reduced Hamaker constant of  $A_r$  should also be chosen relative to the material Hamaker constant  $A_m$  using the correlation  $A_r = A_m \left( E_{R/E_m} \right)^{2/5}$  for a Hertzian model with material Young's modulus  $E_m$  and reduced Young's modulus  $E_R$  or the correlation  $A_r = A_m \left( k_{B/k_m} \right)^{1/2}$  for a linear spring dashpot model with material spring constant  $k_m$  and reduced spring constant  $k_R$  [82,83].

Stiffness sensitivity of our powder bed was tested using 2D LSD and Hertzian simulations up to the material Young's modulus (73 GPa). A consistent correlation between the Young's modulus and the linearized spring stiffness was observed (Figs. B2A, B). Similar to the approach by Kobayashi et al., trends in the spatially averaged particle-particle coordination number were used to quantify the effects of a reduced stiffness and cohesive force on vibratory convection flow behavior,

$$CN_{pp} = \frac{N_{j,pp}}{2N} \tag{B5}$$

where  $N_{i,PP}$  is the number of overlapping particle-particle pairs (neighbors within a radial distance  $r = R_i$  of each particle i) and N is the total number of particles in the system. As observed with fluidized bed simulations [81,83], the coordination behavior of vibrated mildly-cohesive soda lime microspheres changes with spring stiffness when a reduced Hamaker constant is not used (Fig. B3A). "Hard" particles near the material stiffness of 73 GPa were characterized by low average coordination numbers  $CN_{pp}$  and uncoordinated flight periods. By contrast, "soft" particles with stiffnesses under 1.8 GPa (effective spring constants of ~200 N/m or less) were characterized by continuous particle-particle contact  $(CN_{nn} > 0)$ . By contrast, when a reduced spring stiffness is employed with an appropriately reduced Hamaker constant, the coordination network remains relatively insensitive to spring stiffness down to at least k = 3 N/m or E = 0.018 GPa (Fig. B3B). Particle-wall coordination numbers CN<sub>pw</sub> exhibited similar trends with increasing spring stiffness.

To ensure all features of vibrated soda lime glass microspheres are captured accurately, the LSD model at the true material stiffness was used in all remaining simulations (Table 3). LSD model simulations gave similar results to the Hertzian model but with larger time steps, enabling a faster solution, so the LSD model was chosen for modeling fine powder vibratory convection. The small overlap observed in these simulations (below 17 nm or < 0.03% of the particle diameter) is commonly accepted as a valid regime for the linear spring-dashpot model.

#### References

- [1] A.W. Weimer, Particle atomic layer deposition, J. Nanopart. Res. 21 (2019) 9.
- [2] R.L. Puurunen, Surface chemistry of atomic layer deposition: a case study for the trimethylaluminum/water process, J. Appl. Phys. 97 (2005) 9.
- [3] S.M. George, Atomic layer deposition: an overview, Chem. Rev. 110 (2010) 111-131.
- [4] P. Poodt, D.C. Cameron, E. Dickey, S.M. George, V. Kuznetsov, G.N. Parsons, F. Roozeboom, G. Sundaram, A. Vermeer, Spatial atomic layer deposition: A route towards further industrialization of atomic layer deposition, J. Vac. Sci. Technol. A 30 (2012) 010802
- [5] J. McCormick, B. Cloutier, A. Weimer, S. George, Rotary reactor for atomic layer deposition on large quantities of nanoparticles, J. Vac. Sci. Technol. A 25 (2007) 67–74.
- [6] J.R. Wank, S.M. George, A.W. Weimer, Nanocoating individual cohesive boron nitride particles in a fluidized bed by ALD, Powder Technol. 142 (2004) 59–69.
- [7] L.F. Hakim, S.M. George, A.W. Weimer, Conformal nanocoating of zirconia nanoparticles by atomic layer deposition in a fluidized bed reactor, Nanotechnology 16 (2005) \$375.
- [8] D.M. King, J.A. Spencer II, X. Liang, L.F. Hakim, A.W. Weimer, Atomic layer deposition on particles using a fluidized bed reactor with in situ mass spectrometry, Surf. Coat. Technol. 201 (2007) 9163–9171.
- [9] J. Duran, Sands, Powders, and Grains: An Introduction to the Physics of Granular Materials, Springer Science & Business Media, 2012.
- [10] S. Limtrakul, W. Rotjanavijit, T. Vatanatham, Lagrangian modeling and simulation of effect of vibration on cohesive particle movement in a fluidized bed, Chem. Eng. Sci. 62 (2007) 232–245.
- [11] H. Wang, T. Zhou, J.S. Yang, J.J. Wang, H. Kage, Y. Mawatari, Model for calculation of agglomerate sizes of nanoparticles in a Vibro-fluidized bed, Chem. Eng. Technol. 33 (2010) 388–394.
- [12] Y. Mawatari, M. Tsunekawa, Y. Tatemoto, K. Noda, Favorable vibrated fluidization conditions for cohesive fine particles, Powder Technol. 154 (2005) 54–60.
- [13] C.H. Nam, R. Pfeffer, R.N. Dave, S. Sundaresan, Aerated vibrofluidization of silica nanoparticles, AICHE J. 50 (2004) 1776–1785.
- [14] D. Longrie, D. Deduytsche, C. Detavernier, Reactor concepts for atomic layer deposition on agitated particles: A review, J. Vac. Sci. Technol. A 32 (2014) 010802.
- [15] C. Woodcock, J. Mason, Bulk solids handling: an introduction to the practice and technology, Springer Science & Business Media, 2012.
- [16] D. Barletta, M. Poletto, Aggregation phenomena in fluidization of cohesive powders assisted by mechanical vibrations, Powder Technol. 225 (2012) 93–100.
- [17] E. Marring, A.C. Hoffmann, L.P.B.M. Janssen, The effect of vibration on the fluidization behaviour of some cohesive powders, Powder Technol. 79 (1994) 1–10.
- [18] J.R. Wank, S.M. George, A.W. Weimer, Vibro-fluidization of fine boron nitride powder at low pressure, Powder Technol. 121 (2001) 195–204.
- [19] L.F. Hakim, J.L. Portman, M.D. Casper, A.W. Weimer, Aggregation behavior of nanoparticles in fluidized beds, Powder Technol. 160 (2005) 149–160.
- [20] J.M. Valverde, A. Castellanos, Effect of vibration on agglomerate particulate fluidization, AICHE J. 52 (2006) 1705–1714.
- [21] W. Cong, Z. Li, K. Cao, G. Feng, R. Chen, Transient analysis and process optimization of the spatial atomic layer deposition using the dynamic mesh method, Chem. Eng. Sci. 217 (2020) 115513.
- [22] M.B.M. Mousa, J.S. Ovental, A.H. Brozena, C.J. Oldham, G.N. Parsons, Modeling and experimental demonstration of high-throughput flow-through spatial atomic layer deposition of Al2O3 coatings on textiles at atmospheric pressure, J. Vac. Sci. Technol. A 36 (2018), 031517, .
- [23] D. Pan, Numerical study on the effectiveness of precursor isolation using N2 as gas barrier in spatial atomic layer deposition, Int. J. Heat Mass Transf. 144 (2019)
- [24] I.J.A. Spencer, R.A. Hall, Continuous Spatial Atomic Layer Deposition Process and Apparatus for Applying Films on Particles, Google Patents, 2018.
- [25] J.R. van Ommen, D. Kooijman, M.D. Niet, M. Talebi, A. Goulas, Continuous production of nanostructured particles using spatial atomic layer deposition, J. Vac. Sci. Technol. A 33 (2015) 021513.
- [26] J. Booth, H. McCallion, On predicting the mean conveying velocity of a vibratory conveyor, Proceedings of the Institution of Mechanical Engineers, vol. 178, 1963, pp. 521–532
- [27] K. Srinath, R. Karmakar, Vibratory conveying by non-sinusoidal excitation, Proc. Inst. Mech. Eng. C J. Mech. Eng. Sci. 202 (1988) 405–408.
- [28] K. Lonie, A practical model for sub-resonant vibratory feeders, Bulk Solids Handling 3 (1983) 741–746.
- [29] S. MacDonald, B. Stone, An investigation of vibratory feeders, Proceedings of international conference of noise and vibration 1989, pp. 12–26.
- [30] G. Lim, On the conveying velocity of a vibratory feeder, Comput. Struct. 62 (1997) 197–203
- [31] E. Sloot, N.P. Kruyt, Theoretical and experimental study of the transport of granular materials by inclined vibratory conveyors, Powder Technol. 87 (1996) 203–210.

- [32] J. Li, C. Webb, S.S. Pandiella, G.M. Campbell, Discrete particle motion on sieves—a numerical study using the DEM simulation, Powder Technol. 133 (2003) 190–202.
- [33] M. Jahani, A. Farzanegan, M. Noaparast, Investigation of screening performance of banana screens using LIGGGHTS DEM solver, Powder Technol. 283 (2015) 32–47.
- [34] H. Ashrafizadeh, S. Ziaei-Rad, A numerical 2D simulation of part motion in vibratory bowl feeders by discrete element method, J. Sound Vib. 332 (2013) 3303–3314.
- [35] C. Hogue, D. Newland, Efficient computer simulation of moving granular particles, Powder Technol. 78 (1994) 51–66.
- [36] G. Uryadov, A. Katterfeld, F. Krause, DEM Simulation of the Bulk Solid Reaction on Vibratory Conveyors, Bulk Europe, 2008.
- [37] S. Ganapathy, M. Parameswaran, Effect of material loading on the starting and transition over resonance of a vibratory conveyor, Mech. Mach. Theory 22 (1987) 169–176.
- [38] E. Simsek, S. Wirtz, V. Scherer, H. Kruggel-Emden, R. Grochowski, P. Walzel, An experimental and numerical study of transversal dispersion of granular material on a vibrating conveyor, Part. Sci. Technol. 26 (2008) 177–196.
- [39] J.M.V. Millán, Fluidization of fine powders: cohesive versus dynamical aggregation, Springer Science & Business Media, 2012.
- [40] H. Liu, Y. Li, Q. Guo, Fluidization quality improvement for cohesive particles by fine powder coating, Ind. Eng. Chem. Res. 45 (2006) 1805–1810.
- [41] E. Teunou, J. Fitzpatrick, E. Synnott, Characterisation of food powder flowability, J. Food Eng. 39 (1999) 31–37.
- [42] N. Jinapong, M. Suphantharika, P. Jamnong, Production of instant soymilk powders by ultrafiltration, spray drying and fluidized bed agglomeration, J. Food Eng. 84 (2008) 194–205.
- [43] E. Hansuld, L. Briens, A review of monitoring methods for pharmaceutical wet granulation, Int. J. Pharm. 472 (2014) 192–201.
- [44] S.-C. Yang, S.-S. Hsiau, Self-diffusion analysis in a vibrated granular bed, Adv. Powder Technol. 12 (2001) 61–77.
- [45] A. Matchett, T. Yanagida, Y. Okudaira, S. Kobayashi, Vibrating powder beds: a comparison of experimental and distinct element method simulated data, Powder Technol. 107 (2000) 13–30.
- [46] M.F. Llop, F. Madrid, J. Arnaldos, J. Casal, Fluidization at vacuum conditions. A generalized equation for the prediction of minimum fluidization velocity, Chem. Eng. Sci. 51 (1996) 5149–5157.
- [47] Y.I. Rabinovich, J.J. Adler, A. Ata, R.K. Singh, B.M. Moudgil, Adhesion between nanoscale rough surfaces: I. role of asperity geometry, J. Colloid Interface Sci. 232 (2000) 10–16.
- [48] M. Syamlal, W. Rogers, T.J. OBrien, MFIX Documentation Theory Guide, USDOE Morgantown Energy Technology Center, WV (United States), 1993.
- [49] J. Anderson, P.J. Burns, D. Milroy, P. Ruprecht, T. Hauser, H.J. Siegel, Deploying RMACC Summit: an HPC resource for the Rocky Mountain region, Proceedings of the Practice and Experience in Advanced Research Computing 2017 on Sustainability, Success and Impact 2017, pp. 1–7.
- [50] A. Munjiza, P.W. Cleary, Industrial particle flow modelling using discrete element method, Eng. Comput. 26(6) (2009) 698–743.
- [51] P. Liu, T. Brown, W.D. Fullmer, T. Hauser, C. Hrenya, R. Grout, H. Sitaraman, Comprehensive Benchmark Suite for Simulation of Particle Laden Flows Using the Discrete Element Method with Performance Profiles from the Multiphase Flow with Interface eXchanges (MFiX) Code, National Renewable Energy Lab.(NREL), Golden, CO (United States). 2016.
- [52] C. LaMarche, P. Liu, K. Kellogg, C. Hrenya, Fluidized-bed measurements of carefully-characterized, mildly-cohesive (group a) particles, Chem. Eng. J. 310 (2017) 259–271
- [53] C.Q. LaMarche, S. Leadley, P. Liu, K.M. Kellogg, C.M. Hrenya, Method of quantifying surface roughness for accurate adhesive force predictions, Chem. Eng. Sci. 158 (2017) 140–153.
- [54] M. Tahmasebpoor, L. de Martín, M. Talebi, N. Mostoufi, J.R. van Ommen, The role of the hydrogen bond in dense nanoparticle–gas suspensions, Phys. Chem. Chem. Phys. 15 (2013) 5788–5793.
- [55] J.P.K. Seville, C.D. Willett, P.C. Knight, Interparticle forces in fluidisation: a review, Powder Technol. 113 (2000) 261–268.
- [56] J. Dickinson, R. Hariadi, L. Scudiero, S. Langford, A scanning force microscope study of detachment of nanometer-sized particles from glass surfaces, Tribol. Lett. 7 (1999) 113–119.
- [57] J.N. Israelachvili, Intermolecular and surface forces, Academic Press, 2011.
- [58] S.F. Foerster, M.Y. Louge, H. Chang, K. Allia, Measurements of the collision properties of small spheres, Phys. Fluids 6 (1994) 1108–1115.
- [59] P. Liu, C.M. Hrenya, Challenges of DEM: I. competing bottlenecks in parallelization of gas-solid flows, Powder Technol. 264 (2014) 620–626.
- [60] J. Kováčik, Correlation between Young's modulus and porosity in porous materials, J. Mater. Sci. Lett. 18 (1999) 1007–1010.
- [61] J. Kováčik, Correlation between shear modulus and porosity in porous materials, J. Mater. Sci. Lett. 20 (2001) 1953–1955.
- [62] I. Mészáros, Magnetic characterisation of duplex stainless steel, Phys. B Condens. Matter 372 (2006) 181–184.
- [63] K. Kawashima, T. Ito, Y. Nagata, Detection and imaging of nonmetallic inclusions in continuously cast steel plates by higher harmonics, Jpn. J. Appl. Phys. 49 (2010) 07HC11
- [64] A. Redford, G. Boothroyd, Vibratory feeding, Proc. Inst. Mech. Eng. 182 (1967) 135–152.
- [65] S. Okabe, Y. Kamiya, K. Tsujikado, Y. Yokoyama, Vibratory feeding by nonsinusoidal vibration—optimum wave form, 1985.
- [66] S. Nadler, O. Bonnefoy, J.-M. Chaix, G. Thomas, J.-L. Gelet, Parametric study of horizontally vibrated grain packings, Eur. Phys. J. E 34 (2011) 1–10.
- [67] G. Winkler, Analysing the vibrating conveyor, Int. J. Mech. Sci. 20 (1978) 561–570.

- [68] D.C. Kammer, M.L. Tinker, Optimal placement of triaxial accelerometers for modal vibration tests, Mech. Syst. Signal Process. 18 (2004) 29–41.
- [69] A.J. Jerri, The Gibbs phenomenon in Fourier analysis, splines and wavelet approximations, Springer Science & Business Media, 2013.
- [70] M.L. Chandravanshi, A.K. Mukhopadhyay, Dynamic analysis of vibratory feeder and their effect on feed particle speed on conveying surface, Measurement 101 (2017) 145–156.
- [71] R. Schofield, M. Yousuf, The Design of a Linear "out of Phase" Vibratory Conveyor, 1973.
- [72] A. Fukunishi, Y. Mori, Adhesion force between particles and substrate in a humid atmosphere studied by atomic force microscopy, Adv. Powder Technol. 17 (2006) 567–580.
- [73] Y. Gu, A. Ozel, J. Kolehmainen, S. Sundaresan, Computationally generated constitutive models for particle phase rheology in gas-fluidized suspensions, J. Fluid Mech. 860 (2019) 318–349.
- [74] J.M. Parker, A Baseline Drag Force Correlation for CFD Simulations of Gas-Solid Systems, 2016 NETL Workshop on Multiphase Flow ScienceMorgantown, WV, 2016.
- [75] E. Loth, Compressibility and rarefaction effects on drag of a spherical particle, AIAA J. 46 (2008) 2219–2228.

- [76] K.J. Berger, On the Role of Collisions in the Ejection of Lunar Regolith during Spacecraft Landing, University of Colorado, Boulder, 2016.
- [77] E. Dintwa, E. Tijskens, H. Ramon, On the accuracy of the hertz model to describe the normal contact of soft elastic spheres, Granul. Matter 10 (2008) 209–221.
- [78] H.P. Kuo, P.C. Knight, D.J. Parker, Y. Tsuji, M.J. Adams, J.P.K. Seville, The influence of DEM simulation parameters on the particle behaviour in a V-mixer, Chem. Eng. Sci. 57 (2002) 3621–3638.
- [79] Y. Tsuji, T. Tanaka, T. Ishida, Lagrangian numerical simulation of plug flow of cohesionless particles in a horizontal pipe, Powder Technol. 71 (1992) 239–250.
- [80] H.A. Navarro, M.P. de Souza Braun, Determination of the normal spring stiffness coefficient in the linear spring–dashpot contact model of discrete element method, Powder Technol. 246 (2013) 707–722.
- [81] T. Kobayashi, T. Tanaka, N. Shimada, T. Kawaguchi, DEM-CFD analysis of fluidization behavior of Geldart group a particles using a dynamic adhesion force model, Powder Technol. 248 (2013) 143-152.
- [82] K. Washino, E.L. Chan, T. Tanaka, DEM with attraction forces using reduced particle stiffness, Powder Technol. 325 (2018) 202–208.
- [83] Y. Gu, A. Ozel, S. Sundaresan, A modified cohesion model for CFD–DEM simulations of fluidization, Powder Technol. 296 (2016) 17–28.